Structure-Function Analysis of Mammalian CYP2B Enzymes Using 7-Substituted Coumarin Derivatives as Probes: Utility of Crystal Structures and Molecular Modeling in Understanding Xenobiotic Metabolism[S]

Manish B. Shah, Jingbao Liu, Lu Huo, Qinghai Zhang, M. Denise Dearing, P. Ross Wilderman, Grazyna D. Szklarz, C. David Stout, and James R. Halpert

School of Pharmacy, University of Connecticut, Storrs, Connecticut (M.B.S., J.L., L.H., P.R.W., J.R.H.); Department of Integrative Structural and Computational Biology, Scripps Research Institute, La Jolla, California (Q.Z., C.D.S.); Department of Biology, University of Utah, Salt Lake City, Utah (M.D.D.); and Department of Pharmaceutical Sciences, School of Pharmacy, West Virginia University, Morgantown, West Virginia (G.D.S.)

ABSTRACT

Crystal structures of CYP2B35 and CYP2B37 from the desert woodrat were solved in complex with 4-(4-chlorophenyl)imidazole (4-CPI). The closed conformation of CYP2B35 contained two molecules of 4-CPI within the active site, whereas the CYP2B37 structure demonstrated an open conformation with three 4-CPI molecules, one within the active site and the other two in the substrate access channel. To probe structure-function relationships of CYP2B35, CYP2B37, and the related CYP2B36, we tested the O-dealkylation of three series of related substrates—namely, 7-alkoxycoumarins, 7-alkoxy-4-(trifluoromethyl)coumarins, and 7-alkoxy-4-methylcoumarins—with a C1-C7 side chain. CYP2B35 showed the highest catalytic efficiency (k_{cat}/K_M) with 7-heptoxycoumarin as a substrate, followed by 7-hexoxycoumarin. In contrast, CYP2B37 showed the highest catalytic efficiency with 7-ethoxy-4-(trifluoromethyl) coumarin (7-EFC), followed by 7-methoxy-4-(trifluoromethyl) coumarin (7-MFC). CYP2B35 had no dealkylation activity with 7-MFC or 7-EFC. Furthermore, the new CYP2B–4-CPI–bound structures were used as templates for docking the 7-substituted coumarin derivatives, which revealed orientations consistent with the functional studies. In addition, the observation of multiple –Cl and –NH-π interactions of 4-CPI with the aromatic side chains in the CYP2B35 and CYP2B37 structures provides insight into the influence of such functional groups on CYP2B ligand binding affinity and specificity. To conclude, structural, computational, and functional analysis revealed striking differences between the active sites of CYP2B35 and CYP2B37 that will aid in the elucidation of new structure-activity relationships.

Introduction

Cytochrome P450 (P450)–dependent monooxygenases are a superfamily of hemoproteins that play a crucial role in the detoxification and bioactivation of numerous endogenous and xenobiotic compounds, including many drugs, carcinogens, and environmental chemicals (Johnson and Stout, 2013) of diverse size and shape (Ortiz de Montellano, 2015). In mammals, P450 enzymes may have evolved as a defense mechanism to enable adaptation to expanding chemical diversity in the environment (Gonzalez, 1988; Stamp, 2003; Weng et al., 2012). Cytochrome p450 2B subfamily (CYP2B) enzymes were among the first mammalian P450s isolated and cloned and have been characterized in detail in mice, rats, rabbits, dogs, and humans (Domanski and Halpert, 2001; Zhao and Halpert, 2007). Functional differences among various CYP2B enzymes characterized to date have made these enzymes an excellent model system to explore structure-function relationships across species.

Efforts in our laboratory have largely focused on functional, structural, computational, and biophysical approaches to probe interactions of the CYP2B subfamily of proteins with important ligands, including clinically used drugs, small-molecule inhibitors, mechanism-based inactivators, and volatile hydrocarbons. Major accomplishments include determination

ABBREVIATIONS: β-ME, 2-mercaptoethanol; CHAPS, 3-[(3-cholamidopropyl)dimethylammonio]-1-propanesulfonate; CYMAL-5, 5-cyclohexyl-1-pentyl-β-D-maltoside; CYP or P450, cytochrome P450; DTT, dithiothreitol; 4-CPI, 4-(4-chlorophenyl)imidazole; IPTG, isopropyl β-D-1-thiogalactopyranoside; $k$cat, nmoles of product produced per minute per nmole of P450 in the reaction; NaCl, sodium chloride; NMR, nuclear magnetic resonance; 7-PeC, 7-pentoxycoumarin; PMSF, phenylmethylsulfonyl fluoride; 7-EC, 7-ethoxycoumarin; 7-EFC, 7-ethoxy-4-(trifluoromethyl)coumarin; 7-EMC, 7-ethoxy-4-methylcoumarin; 7-HpC, 7-heptoxycoumarin; 7-HxC, 7-hexoxycoumarin; 7-MC, 7-methoxycoumarin; 7-MFC, 7-methoxy-4-(trifluoromethyl)coumarin; 7-PrFC, 7-propoxy-4-(trifluoromethyl)coumarin; rmsd, root-mean-square deviation; 234-chol, 3α-hydroxyl-7α,12α-di-(((2-(trimethylamino)ethyl)phosphoryl)ethyloxy)-cholane.

of over 20 X-ray crystal structures of rabbit CYP2B4 and human CYP2B6, analysis of solution behavior of rabbit CYP2B4 via hydrogen/deuterium exchange coupled to mass spectrometry, and elucidation by isothermal titration calorimetry of solution thermodynamics of ligand binding to CYP2B4 and CYP2B6 (Scott et al., 2004; Muralidhara and Halpert, 2007; Gay et al., 2010a; Halpert, 2011; Shah et al., 2012, 2013b, 2015; Wilderman and Halpert, 2012; Wilderman et al., 2013; Zhang et al., 2013). Computational methods such as ligand docking and molecular dynamics simulations based on X-ray crystal structures as templates have been used to study ligand orientation and interactions within and outside the active site of these CYP2B enzymes (Szklarz et al., 1995; Wilderman et al., 2012; Shah et al., 2013a). In addition, site-directed mutagenesis was crucial to understand the structural and functional role of residues in the active site, access channel, and a recently observed peripheral pocket (Kobayashi et al., 1998; Hernandez et al., 2006; Jang et al., 2014, 2015). Our multifaceted approach has revealed how movement of secondary structure elements, such as the F-G helices and I helix, and reorientation of active-site residues, such as F206 and F297, allow CYP2B enzymes to bind compounds as small as α-pinene (molecular weight = 136 g/mol) and as large as two molecules of amlodipine (molecular weight = 409 g/mol) with high affinity.

Despite the abundant structural and functional information available regarding CYP2B enzymes in multiple species and the hypothesis that these enzymes evolved to deal with plant toxins, the understanding of the role of these detoxification enzymes in nonmodel species or mammalian herbivores is still very limited. Based on evidence that CYP2B enzymes might play a critical role in the ability of the desert woodrat *Neotoma lepida* to survive on native toxic plants (Haley et al., 2007; Malenke et al., 2012), our laboratory recently expressed, purified, and characterized CYP2B35, CYP2B36, and CYP2B37. Functional studies with 7-ethoxy-4-(trifluoromethyl)coumarin (7-EFC) and 7-benzyloxyresorufin as substrates suggested that CYP2B35 had very unusual substrate specificity compared with all previously characterized CYP2B enzymes (Malenke et al., 2012; Wilderman et al., 2014). Amino acid sequence comparisons indicated at least seven active-site positions where the CYP2B35 residue was different from that found in most CYP2B enzymes. The current study further investigates structure-function relationships among CYP2B35, CYP2B36, and CYP2B37 using 7-alkoxycoumarins, 7-alkoxy-4-methylcoumarins, and 7-alkoxy-4-(trifluoromethyl)coumarins with a C1-C7 side chain (Kobayashi et al., 1998) (Supplemental Fig. 1). Concurrently, crystal structures of CYP2B35 and CYP2B37 were solved in complex with 4-(4-chlorophenyl)imidazole (4-CPI) at 2.2 and 3.2 Å, respectively. The structures demonstrate multiple 4-CPI molecules bound, with two in the CYP2B35 complex and three in the CYP2B37 complex. These results are in contrast to previously determined CYP2B4 and CYP2B6 complexes with a single 4-CPI molecule and reveal distinct features within the active site and in the substrate access channel in CYP2B enzymes across various species. Furthermore, ligand docking was employed, using the crystal structures of CYP2B35 and CYP2B37 to evaluate the implications of active-site differences for chain length requirements of *O*-dealkylation of these series of alkoxycoumarins. The experimental results indicate marked differences in substrate selectivity, which were then corroborated by a computational approach based on the new crystal structures of the CYP2B enzymes.

Materials and Methods

Materials. 3-[(3-Cholamidopropyl)dimethylammonia]-1-propane-sulfonate (CHAPS) was obtained from Calbiochem (EMD Chemicals, San Diego, CA). 5-cyclohexyl-1-pentyl-**b**-D-maltoside (CYMAL-5) and isopropyl **b**-D-1-thiogalactopyranoside (IPTG) were obtained from Anatrace (Maumee, OH). Nickel–nitrilotriacetic acid affinity resin was from Thermo Scientific (Rockford, IL). Macro-Prep CM cation exchange resin was received from Bio-Rad Laboratories (Hercules, CA). Amicon ultrafiltration devices were from Millipore (Billerica, MA). The plasmid pGro7 harboring the GroEL/ES chaperones was from Takara Bio (Shiba, Japan). 3α-Hydroxy-7α,12α-di-(((2-(trimethylamino)ethyl)phosphoryl)ethyloxy)-cholane (FA-7/234-chol) is a facial amphiphile used as described previously (Lee et al., 2013). Arabinose, ampicillin, δ-aminolevulinic acid, chloramphenicol, phenylmethylsulfonyl fluoride (PMSF), lysozyme, dithiothreitol (DTT), 2-mercaptoethanol (β-ME), potassium phosphate, sucrose, tryptone, and yeast extract required to prepare Luria-Bertani and Terrific broth medium were purchased from Sigma-Aldrich (St. Louis, MO). Sodium chloride (NaCl), EDTA, and glycerol were from Fisher Scientific (Waltham, MA), and L-histidine was from Spectrum Chemical (New Brunswick, NJ). All protein models were created using PyMol (The PyMOL Molecular Graphics System, version 1.5.0.4; Schrödinger, LLC, New York, NY).

7-Alkoxycoumarins were synthesized by E. Mash (Department of Chemistry, University of Arizona, Tucson, AZ). 7-Hydroxy-4-(trifluoromethyl)coumarin was purchased from Alfa Aesar (Ward Hill, MA). 7-Hydroxy-4-methylcoumarin, 7-methoxy-4-(trifluoromethyl)coumarin (7-MFC), and 7-EFC were purchased from Invitrogen (Carlsbad, CA). American Chemical Society or high-performance liquid chromatography–grade methanol, acetone, acetonitrile, chloroform, ethyl acetate, and n-hexane were purchased from Fisher Scientific. ^{1}H and ^{13}C nuclear magnetic resonance (NMR) spectrum were recorded on a Bruker AVANCE 500 MHz spectrometer (Bruker, The Woodlands, TX) using tetramethyl silane as an internal standard (chemical shifts in δ), and analysis was done on MestReNova software version 8.0.0 (Mestrelab Research, Escondido, CA). Peak multiplicities of NMR signals were designated as *s* (singlet), *d* (doublet), *dd* (doublet of doublet), *t* (triplet), or *m* (multiplet). High-resolution mass spectrometry was performed at the University of Connecticut Mass Spectrometry Facility (Storrs, CT) by Dr. You-Jun Fu on an AccuTOF (JEOL, Peabody, MA) and using a DART (IonSense, Saugus, MA) ionization source. All chemical structures were created using Accelrys Draw software version 4.1 (Accelrys, San Diego, CA).

Chemical Synthesis. All compounds were synthesized in a similar manner according to the published method (Xiaobing et al., 2011; Sánchez-Recillas et al., 2014). A description of synthesis is included in the (Supplemental Material). The purity of the compounds exceeds 95% by ^{1}H NMR.

Protein Expression and Purification. CYP2B35dH, CYP2B36dH, and CYP2B37dH enzymes were expressed in *Escherichia coli* C43 (DE3) competent cells harboring pKK plasmid containing the cDNA for CYP2B35dH, CYP2B36dH, or CYP2B37dH and the pGro7 plasmid that facilitates expression of the GroEL/ES chaperone pair. Enzymes were purified using the protocol described previously (Scott et al., 2001; Shah et al., 2011). An overnight Luria-Bertani broth culture of *E. coli* was used to inoculate Terrific broth containing arabinose (20 mg/ml). Protein expression was induced by the addition of IPTG (1 mM) and δ-aminolevulinic acid (0.5 mM) to Terrific broth medium ($A_{600} \sim 0.7$ at 37°C) containing ampicillin (100 μg/ml) and chloramphenicol (25 μg/ml). The cells were grown for 72 hours at 30°C (190 rpm) prior to harvesting and subsequent centrifugation (4000 × *g*). The pellet was resuspended in buffer containing 20 mM potassium phosphate (pH 7.4 at 4°C), 20% (v/v) glycerol, 10 mM β-ME, and 0.5 mM PMSF and treated with lysozyme (0.3 mg/ml, stirring for 30 minutes), followed by centrifugation for 30 minutes at 7500 × *g*. After the supernatant was decanted, spheroplasts were resuspended in buffer containing 500 mM potassium phosphate (pH 7.4 at 4°C), 20% (v/v) glycerol, 10 mM β-ME, and 0.5 mM PMSF, and

were sonicated for 3×45 seconds on ice. CHAPS was added to the sample at a final concentration of 0.8% (w/v), and the solution was allowed to stir for 30 minutes at 4°C before ultracentrifugation for 1 hour at $245,000 \times g$. The supernatant was collected; the P450 enzyme concentration was determined by measuring a difference spectrum of the ferrous carbonyl complex of the heme protein (Omura and Sato, 1964a,b).

The supernatant was applied to equilibrated nickel–nitrilotriacetic acid resin, and the column was washed with buffer containing 100 mM potassium phosphate (pH 7.4 at 4°C), 100 mM NaCl, 20% (v/v) glycerol, 10 mM β-ME, 0.5 mM PMSF, 0.5% CHAPS, and 5 mM histidine. The protein was eluted using 50 mM histidine, fractions containing protein of the highest quality as measured by the A_{417}/A_{280} ratios were pooled, and the P450 enzyme concentration was measured using the reduced CO difference spectra. Pooled fractions were further diluted 10-fold with buffer containing 5 mM potassium phosphate (pH 7.4 at 4°C), 20% (v/v) glycerol, 1 mM EDTA, 0.2 mM DTT, 0.5 mM PMSF, and 0.5% (w/v) CHAPS and applied to a Macro-Prep CM cation exchange column. The column was washed using 5 mM potassium phosphate (pH 7.4 at 4°C), 20 mM NaCl, 20% (v/v) glycerol, 1 mM EDTA, and 0.2 mM DTT, and the protein was eluted with high-salt buffer containing 50 mM potassium phosphate (pH 7.4 at 4°C), 500 mM NaCl, 20% (v/v) glycerol, 1 mM EDTA, and 0.2 mM DTT. Protein fractions with the highest A_{417}/A_{280} ratios were pooled, and the P450 concentration was measured using the reduced CO-difference spectra.

Enzymatic Assays. The purified proteins were dialyzed in 20 mM phosphate buffer (pH 7.4) containing 20% (v/v) glycerol at 4°C overnight. The reconstituted enzyme system contained purified P450 enzyme, rat NADPH–cytochrome P450 reductase (Harlow et al., 1997), and rat cytochrome $b5$ (Holmans et al., 1994) at a molar ratio of 1:4:2. Reactions were carried out in a 100-μl final volume containing 50 mM HEPES (pH 7.4) and 15 mM MgCl$_2$, 0–200 μM substrate, and the reconstituted enzyme system with a final cytochrome P450 concentration of 0.1 μM at 37°C. The reaction was initiated by the addition of NADPH to a final concentration of 1 mM. For the 7-alkoxycoumarin and 7-alkoxy-4-methylcoumarin series of substrates, the reactions were quenched by adding 25 μl of 2 M HCl after 10 minutes. The O-dealkylated product and substrate were extracted with 450 μl of chloroform, and the product was back-extracted from 300 μl of the chloroform solution using 1.0 ml of 30 mM sodium borate solution (pH 9.2). Fluorescence of products in the borate solution was determined using a Hitachi F2000 fluorescence spectrophotometer (Hitachi, Tokyo, Japan) with excitation at 370 nm and emission at 450 nm for 7-hydroxycoumarin, or excitation at 360 nm and emission at 450 nm for 7-hydroxy-4-methylcoumarin. For 7-alkoxy-4-(trifluoromethyl)coumarin substrates, reactions were quenched by addition of 50 μl of ice-cold acetonitrile after 10 minutes. Fifty microliters of quenched solution was then transferred to a tube containing 950 μl of 0.1 M Tris (pH 9.0). Fluorescence of the product, 7-hydroxy-4-(trifluoromethyl)coumarin, was determined with excitation at 410 nm and emission at 510 nm. Calibration was performed on the same day by measuring the fluorescence intensity of a series of samples containing the same reaction mixture and product at a concentration of 0.5–2 μM. Data were fit to the Michaelis-Menten equation or substrate inhibition equation using Origin (OriginLab, Northampton, MA).

Spectral Binding Studies of 4-CPI Binding to CYP2B35 and CYP2B37. Binding titrations were carried out in buffer containing 50 M potassium phosphate (pH 7.4), 500 mM NaCl, 1 mM EDTA, 0.2 mM DTT, and 500 mM sucrose. Ligand (4-CPI) dissolved in acetone was used at a concentration range from 0 to 10 μM, and total solvent concentration at the end of each titration was less than 1%. Absorbance spectra were recorded at 25°C after the addition of 4-CPI (100 μM stock) to buffer containing 1 μM P450 in a 1-ml reaction volume using an MC2000-2 multichannel CCT rapid-scanning spectrometer (Ocean Optics, Dunedin, FL) using a 1-cm glass cuvette. The data were fit to a derivative of the velocity quadratic equation or "tight binding" equation, $2\Delta A = (\Delta A_{max}/[E_0])((K_S + [I_0] + [E_0]) - (K_S + [I_0] + [E_0])^2 - 4[E_0][I_0])^{1/2})$, where E_0 is total enzyme concentration and I_0 is total inhibitor concentration when data are normalized to total P450

concentration (Segel, 1975). 4-CPI was chosen for crystallization experiments due to its high affinity to both CYP2B4 and CYP2B6 and published high-resolution X-ray crystal structures in complex with both CYP2B4 and CYP2B6. Spectral titrations yielded a K_S of 2.3 and 2.0 μM for CYP2B35 and CYP2B37, respectively.

Crystallization and Data Collection. The eluted fractions of pure CYP2B35 or CYP2B37 from the CM column were pooled and further diluted to 18 μM in 50 mM potassium phosphate (pH 7.4 at 4°C), 500 mM NaCl, 500 mM sucrose, 1 mM EDTA, and 0.2 mM DTT. The inhibitor 4-CPI was added to a final concentration of 180 μM, and the samples were concentrated to 550 μM by centrifugation using 50 kDa cutoff Amicon ultrafiltration devices. The protein was again diluted to 18 μM using the aforementioned buffer containing 180 μM 4-CPI, and the process was repeated twice before concentrating CYP2B35 or CYP2B37 to the final concentration of 550 μM. The samples were then supplemented with 4.8 mM CYMAL-5 and 0.044% (w/v) 234-chol, and filtered via 0.22 μm ultrafree centrifugal filters (EMD Millipore, Billerica, MA) prior to crystallization using the sitting drop vapor diffusion method. The crystals of CYP2B35 were obtained over a period of 5–7 days at 18°C from Rigaku Wizard-2 (Rigaku, Bainbridge Island, WA) and Molecular Dimensions Clear Strategy Screen II (Molecular Dimensions, Altmonte Springs, FL) in conditions containing 30% (v/v) polyethylene glycol 400, 0.1 M Hepes (pH 7.5), and 0.2 M NaCl (Rigaku), and 0.2 M calcium acetate, 0.1 M Tris (pH 8.5), and 15% w/v polyethylene glycol 4000 (Molecular Dimensions). CYP2B37 crystallized after 15 days of incubation with 4-CPI at 18°C in 0.1 M Bis-Tris (pH 6.5) and 45% Polypropylene Glycol P400 from the Hampton Research (Aliso Viejo, CA) Index screen. Crystals of CYP2B35 and CYP2B37 were transferred to the mother liquor containing 20% sucrose for cryoprotection before flash freezing in liquid nitrogen. Crystallographic data were collected remotely at Stanford Synchrotron Radiation Lightsource (Menlo Park, CA) using beam lines 12-2 and 11-1 for CYP2B35 and CYP2B37 crystals, respectively, with a PILATUS 6M detector. As the CYP2B35–4-CPI crystals begin to decay in the X-ray beam, each of the data sets for crystals grown in the previous two conditions were collected using 0.5° oscillations over 120 frames and 1-second exposure at 100 K. Images were integrated using iMosflm (Battye et al., 2011), and the two integrated portions were merged in CCP4i and scaled using SCALA (Bailey, 1994). CYP2B37 data sets were collected using 1° oscillations over 240 frames and 20-second exposure at 100 K, and further integrated and scaled using iMosflm and SCALA, respectively.

Structure Determination and Refinement of CYP2B35 and CYP2B37 in Complex with 4-CPI. The structures of CYP2B35 and CYP2B37 in complex with 4-CPI were solved at 2.4- and 3.4-Å resolution, respectively, using the previously determined CYP2B4–4-CPI complex (Protein Data Bank identifier 1SUO with 4-CPI removed from the structure coordinates) via the Phaser molecular replacement program from the CCP4 suite (McCoy et al., 2007). The CYP2B35–4-CPI complex structure solution was found in space group P_1 with 57.5% solvent content and six molecules per asymmetric unit. Iterative refinement was performed in Refmac5 (Murshudov et al., 1997) followed by model building in COOT (Emsley and Cowtan, 2004) using $2F_o$-F_c and F_o-F_c electron density maps contoured to 1-σ and 3-σ, respectively. The R-factor of 0.21 and R-free of 0.28 were achieved for the CYP2B35–4-CPI complex, and the final model with six chains contained 12 4-CPI, two CYMAL-5, four glycerol, one sucrose, and over 600 water molecules.

The Matthews coefficient for the CYP2B37 structure suggested the presence of one molecule per asymmetric unit in the I_4 space group with 75% solvent content. The data were uploaded to the UCLA diffraction anisotropy server and determined to have mild anisotropy of 19.67 A^2 based on the spread in values of the three principal components (Strong et al., 2006). The output scaled data set was used for refinement using Refmac5 (Murshudov et al., 1997), followed by model building in COOT using $2F_o$-F_c and F_o-F_c maps contoured at 1-σ and 3-σ, respectively. Iterative model building and refinement was continued until the R-factor of 0.21 and R-free of 0.29 were achieved.

A total of 16 water molecules were observed in the CYP2B37 structure, and residues from 29 to 491 were present in the final model of the CYP2B37–4-CPI complex. MOLPROBITY (http://molprobity.biochem. duke.edu/; Davis et al., 2004) ranked the CYP2B35–4-CPI and CYP2B37–4-CPI structures at the 92nd and 90th percentiles, respectively, with overall geometry compared with other structures at a similar resolution.

Molecular Modeling Simulations. All molecular modeling was performed on an SGI Octane workstation with an Insight II/Discover software package (Accelrys) using a consistent valence force field supplemented with parameters for heme (Paulsen and Ornstein, 1991, 1992). Alkoxycoumarin substrates, including 7-methoxycoumarin (7-MC), 7-ethoxycoumarin (7-EC), 7-propoxycoumarin, 7-butoxycoumarin, 7-pentoxycoumarin (7-PeC), 7-hexoxycoumarin (7-HxC), 7-heptoxycoumarin (7-HpC), 7-ethoxy-4-methylcoumarin (7-EMC), and 7-ethoxy-4-(trifluoromethyl)coumarin, were built and energy minimized using the Builder module of Insight II. All 4-CPI and water molecules were removed from each of the CYP2B35 and CYP2B37 structures prior to simulations. The X-ray crystal structures of CYP2B35 and CYP2B37 were prepared for molecular dynamics simulations by the addition of hydrogens and subsequent energy minimization (Huang and Szklarz, 2010). The ligands were initially placed manually into the active site of the enzyme in binding orientations consistent with O-dealkylation using the Docking module of Insight II, as described previously (Szklarz et al., 1995; He et al., 1997; Szklarz and Paulsen, 2002). To find the optimal ligand conformation, a dynamic docking approach was used, in which the substrate and the enzyme residues within 5 Å from the substrate were allowed to move, and a 5-Å distance restraint was imposed between the heme iron and the carbon of the substrate where oxidation would take place. The enzyme-substrate complex was subjected to 1000 steps of minimization using steepest descent followed by 1 ps molecular dynamics simulations at 300 K in vacuo using distant-dependent dielectric to remove van der Waals overlaps (Kent et al., 1997; Strobel et al., 1999). The resulting trajectory was analyzed to find the best substrate orientation, and the enzyme-substrate complex was minimized for another 1000 steps, as described earlier. This optimal substrate orientation was used as a starting point for automated docking with the Affinity module of Insight II using default parameters, as described earlier (Ericksen and Szklarz, 2005; Tu et al., 2008; Huang and Szklarz, 2010; Walsh et al., 2013). Residues within 10 Å from the initial substrate position comprised the flexible region of the protein during all docking runs. Twenty distinct binding complexes (substrate heavy atom rmsd exceeding 1.0 Å) obtained by the Monte Carlo search technique were subjected to simulated annealing prior to energy ranking. The simulated annealing consisted of 50 steps, with the temperature ranging from the initial 500 K to a final 300 K. This was followed by 1000 steps of conjugate gradient minimization, as recommended by the standard protocol using Affinity Release 98 (Molecular Simulations Inc, San Diego, CA). Ten lowest-energy binding orientations were then selected for further analysis. The most energetically favorable enzyme-ligand complex was chosen to represent the binding orientation of the substrate, and a productive orientation was defined as a pose in which the distance between the heme iron and the carbon at the oxidation site was less than 5–6 Å.

Results

Screen for 7-Alkoxycoumarin O-dealkylation Activity. CYP2B35, CYP2B36, and CYP2B37 display markedly different O-dealkylation profiles with the canonical CYP2B substrates 7-EFC and 7-benzyloxyresorufin (Wilderman et al., 2014). CYP2B35 has no activity toward either substrate, and CYP2B36 is not active with 7-benzyloxyresorufin and is much less active than CYP2B37 with 7-EFC. In an effort to identify substrates for CYP2B35 and to characterize the enzymes

further, a screen for O-dealkylation of three series of 7-alkoxycoumarins was performed, and the activity as a function of the length of the alkyl chain was recorded (Supplemental Fig. 2). At the concentration of substrate used for screening (200 μM), CYP2B35 metabolizes long-chain substrates and has no activity with short-chain substrates, whereas CYP2B36 and CYP2B37 exhibit the highest apparent activity with substrates containing one-carbon and two-carbon alkoxy chains, respectively.

Steady-State Kinetics Analysis of Select Substrates. To further investigate the distinct substrate chain length preference of CYP2B35 and CYP2B37, steady-state kinetic parameters were obtained with the following six substrates: 7-MFC, 7-EFC, 7-propoxy-4-(trifluoromethyl)coumarin (7-PrFC), 7-PeC, 7-HxC, and 7-HpC (Supplemental Table 1). For 7-MFC, 7-EFC, and 7-PrFC, CYP2B35 had no detectable O-dealkylation activity, and CYP2B37 displayed the greatest catalytic efficiency with 7-EFC followed by 7-MFC and 7-PrFC (Fig. 1A). For the long-chain alkoxycoumarin substrates, CYP2B35 displayed increasing catalytic efficiency as the alkoxy chain became longer (Fig. 1B). CYP2B35 showed substrate inhibition with 7-PeC and 7-HxC, with K_i values of 14.1 and 103.5 μM, respectively, but substrate inhibition was not seen with 7-HpC. Representative steady-state kinetic curves for 7-PeC and 7-HpC O-dealkylation by CYP2B35 are shown in Fig. 2. Due to the decrease in substrate inhibition and the gradual increase in catalytic efficiency with increasing length of the alkyl chain, 7-HpC is the best substrate for CYP2B35. Whereas CYP2B37 displayed much lower k_{cat} (nmoles of product produced per minute per nmole of P450 in the reaction) values than CYP2B35 with 7-PeC, 7-HxC, and 7-HpC, catalytic efficiencies with 7-PeC and 7-HxC are close to those seen with CYP2B35 (Fig. 1B).

Structures of CYP2B35 and CYP2B37 in Complex with 4-CPI. The six chains (chains A–F) found in the crystal structure of CYP2B35 in complex with 4-CPI were identical to
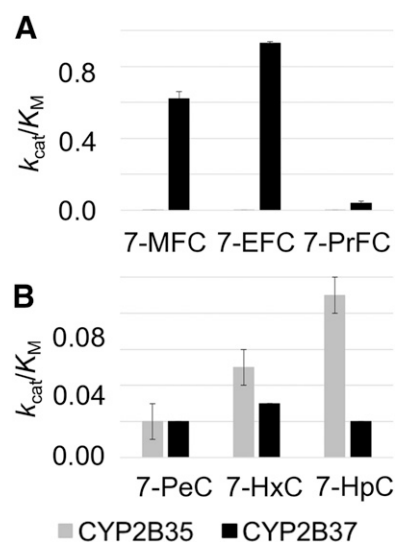

Fig. 1. Catalytic efficiencies (k_{cat}/K_M) for O-dealkylation of select substrates by CYP2B35 and CYP2B37. (A) Comparison of catalytic efficiency of 7-MFC, 7-EFC, and 7-PrFC metabolism versus chain length. (B) Comparison of catalytic efficiency of 7-PeC, 7-HxC, and 7-HpC metabolism versus chain length. Values are depicted as catalytic efficiency ± standard deviation and are taken from Supplemental Table 1.
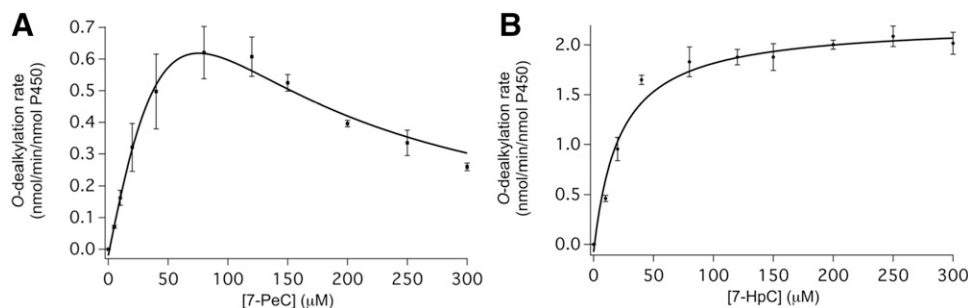
Fig. 2. Representative curves showing steady-state kinetic analysis of 7-PeC versus 7-HpC *O*-dealkylation by CYP2B35. Kinetic data were collected for CYP2B35 as described in the *Materials and Methods* section. The k_{cat}, K_M, and K_i values determined are shown in Supplemental Table 1. Data for 7-PeC (A) display substrate inhibition, whereas data for 7-HpC *O*-dealkylation (B) were fit to the Michaelis-Menten equation without substrate inhibition. The points and the error bars reflect the mean and the standard deviation, respectively, from three independent experiments.

each other, with an average Cα root-mean-square deviation (rmsd) of ~0.25 Å between each chain. An unbiased electron density for 4-CPI corresponding to imidazole nitrogen-heme-iron ligation was present in the active site (Supplemental Fig. 3A). In addition, a similar unbiased electron density corresponding to another molecule of 4-CPI was present in the void region near residues A363 and A367 and perpendicular to the first molecule within the active site. The structure of CYP2B37 with one molecule in the asymmetric unit demonstrated an unbiased electron density for 4-CPI that corresponded to imidazole nitrogen-heme-iron ligation in the active site (Supplemental Fig. 3B). Furthermore, an unbiased electron density corresponding to a second 4-CPI molecule was observed near the β₄ loop region in close proximity to the first 4-CPI, positioning itself at the periphery of the active site and in the previously identified substrate access channel *2f* (Shah et al., 2012). An unbiased electron density was identified for a third 4-CPI molecule at the entrance of the substrate access channel close to the protein surface and sandwiched between helices A′ and F′. Electron density for several residues or the side chain of residues from 135 to 139 and the C-terminal histidines were disordered, and were thus not modeled in the final structure of CYP2B35 and CYP2B37. The CYP2B35–4-CPI and CYP2B37–4-CPI complex coordinates and structure factors were deposited in the Protein Data Bank (Protein Data Bank identifier 5E58 and 5E0E, respectively). Data collection and refinement statistics along with Ramachandran analysis are shown in Table 1.

Comparison of 4-CPI Complexes of CYP2B35 and CYP2B37. Overlay of CYP2B35 and CYP2B37 structures revealed significant differences in the overall conformation of the protein and within the active site. The two structures superimpose onto each other with an average Cα rmsd of ~1.2 Å. As shown in Fig. 3A, the CYP2B35–4-CPI complex demonstrated a closed conformation of the protein identical to that observed with CYP2B4 and CYP2B6 in complex with 4-CPI. In contrast, the CYP2B37 structure in the presence of three molecules of 4-CPI represents an open conformation similar to that observed in the dual ligand complexes of CYP2B4 and CYP2B6 with amlodipine. The previously identified substrate access channel *2f* in the CYP2B4 and CYP2B6 structures is also represented in Fig. 3A, illustrating the location and pathway of multiple 4-CPI molecules in the open conformation of the CYP2B37 structure. Relative to the closed CYP2B35 structure, the CYP2B37 complex exhibits a substantial displacement (3–5 Å) of the F-G cassette and of helices

A′ and A. The residues from S211 to P228 in the F′ and G′ helix region in the F-G cassette were displaced by around 5 Å, most likely to accommodate multiple ligand molecules along and at the tip of the access channel.

Furthermore, the amino acid sequence differences between the two enzymes yield alternate active-site architectures. In the CYP2B35 active site, a total of 19 residues were located within 5 Å from either 4-CPI molecule, as shown in Fig. 3B. These include R98, I101, I104, I108, L114, F115 near the B′ helix region, F206 and M209 (F helix), S294, F297, A298, T302 located on the I helix, and L362, A363, G366, A367, P368 surrounding helix K, and I477 and G478 of the β₄ loop. Residues 363 and 367 are alanine in the active site of CYP2B35, as opposed to L363 and V367 in human CYP2B6, and I363 and V367 in CYP2B4 and CYP2B37. These amino acid differences allow room for CYP2B35 to accommodate another 4-CPI molecule in the void region between the heme-ligating 4-CPI molecule and A363 and A367. The chloro group of this second 4-CPI molecule sits between the side chains of A367 and I114, facing the side chains of R98 and F115. The side chains of T302, L362, A363, and I477 surround the imidazole ring of the second 4-CPI molecule, and the imidazole nitrogen is within hydrogen bonding distance from the free nitrogen in the first 4-CPI molecule (Fig. 3B). Residues V104, M209, and I477 form a "roof" that closes the active site in the CYP2B35 complex. However, these residues in CYP2B37 are instead I104, I209, and F477, and are displaced considerably due to the second molecule of 4-CPI located at the active-site periphery and into the substrate access channel *2f* (Fig. 3, A and C).

In the CYP2B37 structure, nine residues are located within 5 Å from the single 4-CPI molecule in the active site coordinated to the heme-iron: I101, V114, F115, F297, A298, G299, T302, I363, and V367 (Fig. 3C). The residues closer to the second 4-CPI molecule observed in Fig. 3C included E218 (F′ helix), I365, P368, Y389, and F477, which are predominantly within the *2f* substrate access channel region. The side chain of F477 was disordered at the given resolution, and thus was not modeled in the structure. Residues within 5 Å from the third 4-CPI molecule were L43, M46, D47, and F51 of the A′ and A helices, and F212 and Q215 of the F′ helix (Fig. 3C), which are located near the surface at the substrate access region of the channel *2f*. Furthermore, in the CYP2B37 complex, the orientation of the active-site 4-CPI molecule is the same as that previously observed in the CYP2B4 and CYP2B6 structures. However, the 4-CPI molecule coordinated to the heme iron in the CYP2B35 structure rotates toward the I helix by ~90°

TABLE 1
Data collection and refinement statistics

Construct	CYP2B35	CYP237
Ligand	4-CPI	4-CPI
Crystal space group	$P1$	$I4_1$
Crystal unit cell parameters (Å)		
A	98.0	144.77
B	106.1	144.77
C	106.1	104.47
α (°)	64.6	90
β (°)	82.5	90
γ (°)	69.9	90
Data collection statistics (values for highest resolution shell are shown in parentheses)		
Beam line	SSRL 7-1	SSRL 11-1
Wavelength (Å)	0.98	0.97
Resolution range (Å)	40–2.4 (2.46–2.4)	102.6–3.4 (3.48–3.4)
Completeness (%)	94.9 (81.5)	97.8 (91.9)
Redundancy	6.7 (6.3)	3.9 (4.1)
R_{merge}	0.23 (0.9)	0.11 (0.48)
I/σ	6.8 (2.0)	6.2 (1.6)
No. of observations	1,072,927	93,065
No. of unique reflections	16,1098	23,617
Refinement statistics (values for highest resolution shell are shown in parentheses)		
R-factor (%)	21 (29)	21 (34)
R_{free} (%)	28 (35)	29 (36)
RMS deviations		
Bond lengths (Å)	0.01	0.01
Bond angles (°)	1.7	1.8
Average B factor (Å^2)	44.8	86.27
Ramachandran plot		
Favored (%)	96	79
Outliers (%)	0.3	0.7
Number of atoms		
Protein[a]	21,898 (47.9)	3593 (89.9)
Heme[a]	258 (32.2)	43 (60.2)
Solvent[a]	659 (39.4)	16 (55.5)
Ligands[a]		
4-CPI	144 (54.0)	36 (102.1)
Sucrose	23 (53.5)	—
Glycerol	24 (61.9)	—
CYMAL-5	18 (62.7)	—

R_{merge}, $\sum hkl \sum i |Ihkl - <Ihkl>|/\sum hkl \sum iIhkl$, where Ihkl is the intensity of a measurement of the reflection with indices h, k and l and $<Ihkl>$ is the mean intensity of redundant measurements of that reflection; SSRL, Stanford Synchrotron Radiation Lightsource.
[a]Average B-factors (Å^2) are in parentheses.

(Fig. 3D) to accommodate the neighboring 4-CPI molecule in the active site. In addition, the crucial residue side chains F206 and F297 in the CYP2B37 structure are in similar orientation as that observed in the 4-CPI complexes of the CYP2B4 and CYP2B6 structures. As shown in Fig. 3D, these residues in CYP2B35 now rotate by 90° around the axis to an alternate orientation, likely in response to the movement of the 4-CPI molecule ligated to the heme iron toward the I helix.

Analysis of Active-Site Volume. The active-site volume of CYP2B35 and CYP2B37 in complex with 4-CPI was calculated using Voidoo (Kleywegt and Jones, 1994; Uppsala Software Factory, Uppsala, Sweden), and the differences were interpreted in light of previously analyzed active-site volumes of CYP2B4 and CYP2B6 complexes. Eight cycles of cavity detection were performed with Voidoo using a probe occupied option with a probe radius of 1.40 Å (Kleywegt and Jones, 1994). The closed conformation structure of the CYP2B35–4-CPI complex yielded an active-site volume of 495 A^3 (Fig. 4A), whereas the open conformation structure of CYP2B37–4-CPI with the active site extending in to the access channel revealed a volume of 639 A^3 (Fig. 4B). The latter calculation is valid only when the second 4-CPI molecule at the periphery of the active site and in the access channel is included. Closing the "roof" of

the active site by excluding the second 4-CPI molecule significantly reduced the size of the CYP2B37 binding cavity to 469 A^3 (Fig. 4C). The cavity volume was recalculated after adding water molecules at the location of the second 4-CPI to avoid what has been referred to as the "leaking effect," where the cavity extends into the region outside of the active site (Cuff and Martin, 2004). The new volume is comparable to, but slightly smaller than, the cavity volume of CYP2B35 complexed with two molecules of 4-CPI. Despite the smaller side chains of several key residues in CYP2B35 compared with CYP2B37, the differences in orientation of other crucial residue side chains in the CYP2B35 active site limited the size of the binding pocket to 495 A^3.

As seen in Fig. 4, A and C, the differences mainly include orientation of the F206 side chain, which rotates in to the CYP2B35 active site, thereby blocking the extra subchamber that is observed in the CYP2B37 structure where the same F206 side chain flips out of the active site. Furthermore, the F206 side chain in the CYP2B37–4-CPI complex is superimposable onto the previously determined CYP2B6–4-CPI complex, where the outward orientation contributed to an increased active-site volume (582 A^3) in the human enzyme (Gay et al., 2010b). Also, the CYP2B37-F206 side chain overlays well onto
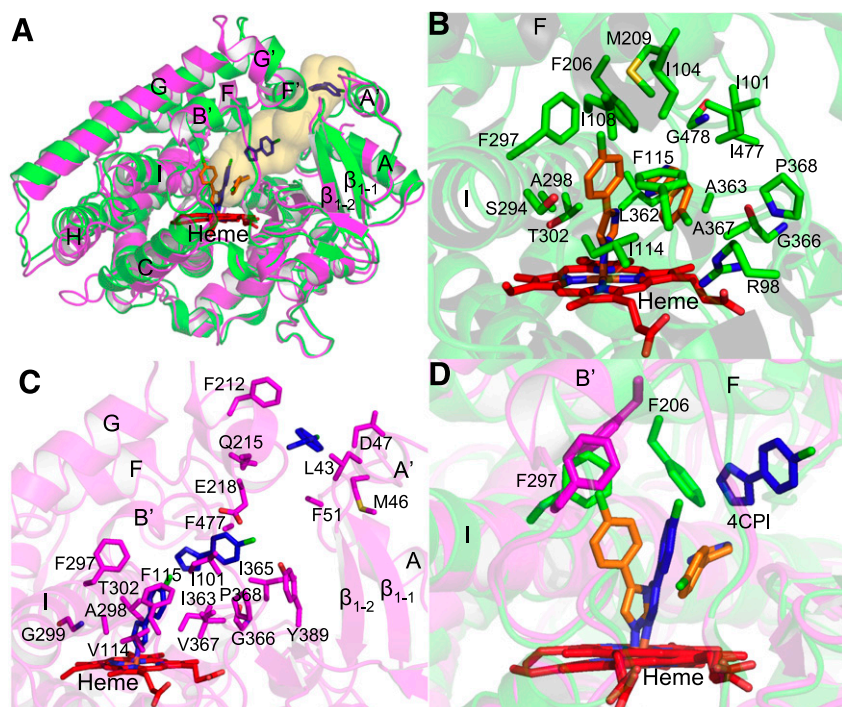
Fig. 3. (A) Overlay of CYP2B35 (green) and CYP2B37 (magenta) structures showing closed and open conformations, respectively. The 4-CPI molecules in the CYP2B35 structure are shown as orange sticks, and those in the 2B37 structure, as blue sticks. Substrate access channel *2f* is shown in pale yellow extending to the protein surface from heme. (B) Active site of the CYP2B35 structure (green) showing residues located within 5 Å from either 4-CPI molecule (orange sticks). A total of 19 residues that include A363 and A367 are shown, constituting the active site of CYP2B35. (C) The residues that comprise the active site in the CYP2B37 structure (magenta) within 5 Å from the 4-CPI (blue) coordinating heme are I101, V114, F115, F297, A298, G299, T302, I363, and V367, represented as sticks. The residues within 5 Å from the second and third 4-CPI molecules located in the access channel are also shown as sticks. (D) Alternate orientation and rearrangement of F206 and F297 side chains in the CYP2B35 (green) and CYP2B37 (magenta) structures are represented as sticks. The reorientation of the 4-CPI toward the I helix and the adjacent molecule in the CYP2B35 active site are shown as orange sticks. The 4-CPI molecules, one located within the active site and the other at the periphery, in the CYP2B37 structure are shown in blue.

the F206 side chain of the CYP2B4 complexed with 4-CPI. However, the cavity volume in the rabbit enzyme was significantly reduced to 253 A³ (Gay et al., 2010b) mainly as a result of the E301 side chain protruding into this extra space observed in the CYP2B6–4-CPI and CYP2B37–4-CPI complexes. The same E301 side chain on the I helix in CYP2B35 sways out by >3.5 Å compared with CYP2B37, likely due to the rotation of 4-CPI coordinating heme toward the I helix, which also contributes to the increase in the active-site volume of CYP2B35.
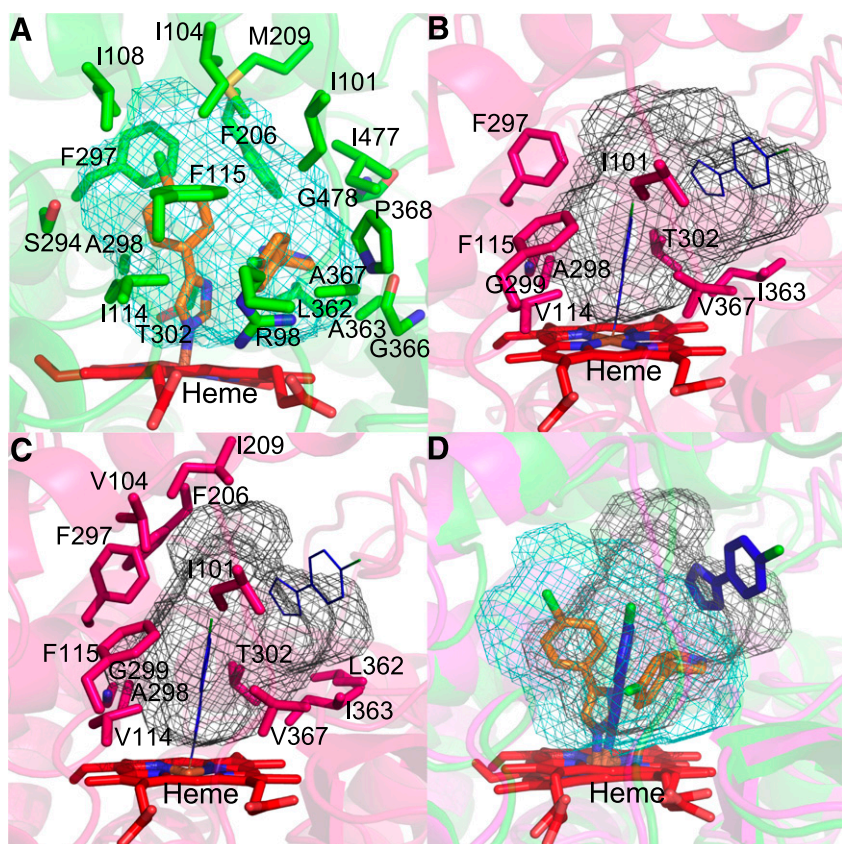

Fig. 4. Active-site cavity volume representation of CYP2B35 (green) and CYP2B37 (magenta). (A) The active-site volume (495 A³) of the CYP2B35 structure is shown in cyan mesh. The important residue substitutions A363 and A367 that contribute to the enlarged binding cavity and two 4-CPI molecules (orange sticks) are also shown. (B) The CYP2B37 active-site volume including the second 4-CPI molecule calculated as 639 A³ and represented in black mesh. Active-site residue side chains with 5 Å from the 4-CPI molecules (blue lines) are shown as sticks. (C) Active-site cavity volume (469 A³) measured excluding the second 4-CPI molecule located at the periphery of the active site and the access channel. Residue side chains of V104, F206, I209, and L362 that contribute to the subcavities or pockets in the CYP2B37 structure are also shown. (D) Differences in the cavity volume between the upper half and the lower half of the active site in CYP2B35 and CYP2B37 structures are represented in mesh overlay. The 4-CPI molecules in the respective structures are shown as sticks.

Molecular Modeling to Understand 7-Alkoxycoumarin *O*-Dealkylation Preference. The CYP2B35 and CYP2B37 structures not only represent alternate active sites in the presence of 4-CPI, but also vary in the overall conformation of the protein and the number of ligand molecules bound to the respective enzymes. Therefore, it was crucial to elucidate whether the active site and the overall conformation observed in the crystallographic structures are adaptable to docking of other ligands. A diverse set of ligands from the three series of alkoxycoumarins were docked into the active site of CYP2B35 or CYP2B37 structures, while allowing active-site residues to remain flexible. The resulting orientations of these ligands obtained from computational docking were compared with the experimental evidence concerning the known site of *O*-dealkylation.

Thus, selected 7-alkoxycoumarin substrates with varying alkoxy chain lengths from 7-MC to 7-HpC were docked into the X-ray crystal structures of CYP2B35 and CYP2B37. In the case of CYP2B35, the analysis of the 10 lowest energy poses (97–130 kcal/mol) for 7-EC docked in the active site of the enzyme revealed that none of the binding orientations obtained was conducive to *O*-dealkylation at the proposed oxidation site (O1 atom), with the distance from the heme iron being around 7 Å or more. Figure 5A shows the lowest energy pose for 7-EC docked in the active site of CYP2B35. In contrast, the CYP2B37 active site revealed preference for shorter-chain 7-alkoxycoumarins, in particular 7-EC, which demonstrates an orientation consistent with dealkylation. All 10 poses for 7-EC docked in the CYP2B37 active site were fairly close in energy (401–410 kcal/mol), and six out of 10 assumed orientations that may allow for catalysis, with the proposed oxidation site within a distance of 5–6 Å from the heme iron (Fig. 5B). The 7-EC in CYP2B35 flipped by 180° along the ligand (C4–C6) axes, but the plane of the ligand was the same as that of 7-EC in the CYP2B37 structure. The CYP2B35 structure revealed preference for longer-chain 7-alkoxycoumarins, in particular 7-HpC (188–220 kcal/mol). Four out of 10 poses for 7-HpC docked in the CYP2B35 active site demonstrated orientations consistent with *O*-dealkylation at the O1 atom (Fig. 5C). In contrast, in the case of CYP2B37, none of the 10 poses (binding energies 388–421 kcal/mol) would allow for substrate oxidation, as C1 was very far (>8 Å) from the heme iron. The lowest energy pose for 7-HpC is shown in Fig. 5D. Furthermore, for 7-MC and 7-propoxycoumarin, only three and two poses, respectively, demonstrated orientations consistent with metabolism, whereas for 7-butoxycoumarin and 7-PeC, only one pose was consistent with substrate metabolism (not shown). Interestingly, docking of 7-EFC into the CYP2B35 crystal structure did not reveal a single pose out of 10 lowest-energy orientations (126–147 kcal/mol) that would be close enough to the heme iron to facilitate catalysis (Fig. 5E). On the other hand, in the CYP2B37 structure, 7-EFC docked (binding energies 400–421 kcal/mol) with at least three possible poses that may represent orientations favorable for catalysis, as shown in Fig. 5F. Accordingly, Fig. 5, E and F illustrates a representative pose for 7-EFC docked in the CYP2B35 and CYP2B37 structures with ligand (C8–O1) axes rotated away from the heme iron in CYP2B35. Additionally, 7-EMC with a methyl group at the C4 position was also docked in the active sites of the enzymes. Two out of 10 binding orientations obtained with CYP2B37 (Fig. 5H) favored catalysis as opposed to only one such orientation observed for CYP2B35 (Fig. 5G). The lowest-energy binding
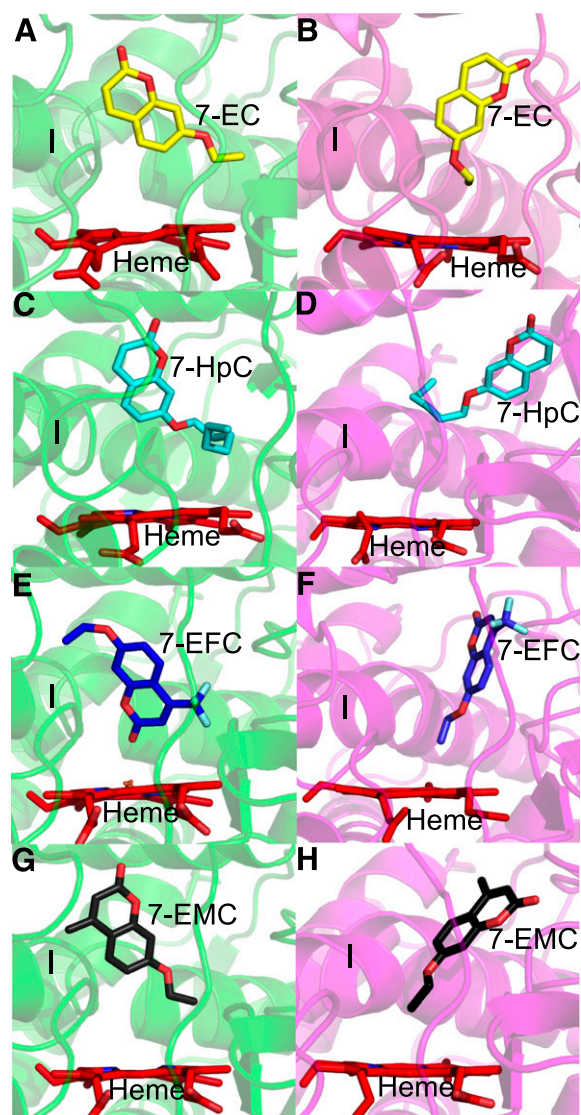

Fig. 5. 7-Substituted coumarin derivatives docked into CYP2B35 (green) and CYP2B37 (magenta) crystal structures (left and right panels, respectively). The lowest-energy pose for each substrate is shown. (A) Representative pose of 7-EC (yellow) in the CYP2B35 structure. (B) Docking of 7-EC in CYP2B37 revealed poses with a proposed oxidation site closer to the heme. (C and D) 7-HpC (cyan) demonstrated an orientation consistent with proposed metabolism in the CYP2B35 structure, whereas an alternate orientation was observed in the CYP2B37 active site, with the oxidation site far from the heme. (E and F) Docking of 7-EFC (blue) in the CYP2B35 and CYP2B37 structures, illustrating the lowest-energy pose with the proposed catalytic orientation observed only in the CYP2B37 structure. (G and H) Docking of 7-EMC (black) in the CYP2B35 and CYP2B37 structures.

orientation of 7-EMC in CYP2B35 was perpendicular to its orientation in the CYP2B37 structure, with the oxidation site further away from heme iron. The aforementioned analyses confirm the utility of the crystal structures obtained in complex with 4-CPI for investigating enzyme metabolism with other substrates, as well as evaluation of catalytic orientations in light of the experimental results.

Discussion

Almost all knowledge on the interactions of mammalian P450 enzymes with substrates stems from studies of the
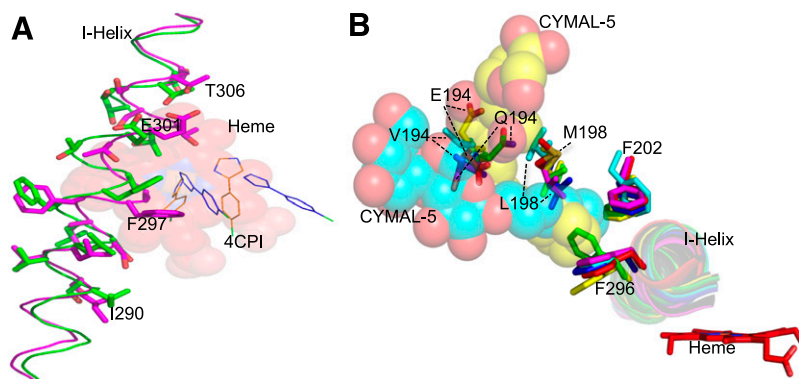
Fig. 6. (A) An overlay of the I helix in the CYP2B35 (green) and CYP2B37 (magenta) structures. The 4-CPI molecules in CYP2B35 are represented as orange lines, and in CYP2B37, as blue lines. A kink in the I helix (residue side chains 290–306 as sticks) is observed in the CYP2B35 structure likely as a result of the rotation of 4-CPI coordinating heme. This rotation leads to rearrangement of several residues in the active site, including the crucial residue side chains of F297 and E301. (B) Overlay of peripheral pocket residue side chains 194, 198, 202, and 296 in stick representation from the structures of CYP2B35–4-CPI (green), CYP2B37–4-CPI (magenta), CYP2B4–4-CPI (blue), CYP2B6–α-pinene (yellow), CYP2B6-amlodipine (red), and CYP2B4-paroxetine (cyan). CYMAL-5 from the CYP2B6–α-pinene and CYP2B4-paroxetine structures is shown in yellow and cyan spheres, respectively. Heme is shown in red sticks, and the I helix in ribbon.

metabolism of drugs rather than studies on species that commonly encounter toxins in nature. In this study, we compared the structure and function of two CYP2B enzymes with ~92% amino acid sequence identity from a mammalian herbivore (*N. lepida*) that naturally ingests high levels of toxins, including monoterpenes, produced by plants in its diet (Malenke et al., 2012). The results revealed differences in the preferences and abilities of these enzymes to metabolize model substrates that are likely related to differences in the size of the active sites. The observed variation in the function of these enzymes presumably enables the metabolism of a multitude of toxins present in the diet.

The CYP2B35 and CYP2B37 crystal structures revealed significant differences in the overall conformation and in the active-site adaptation upon binding multiple 4-CPI molecules. The binding of the second 4-CPI within the active site of CYP2B35 leads to the rotation of the 4-CPI molecule coordinating to heme toward the I helix, and distorts the secondary structure in the helical region containing residues I290–I305 by 1–4 Å. Residues F297–E301 are translated by ~3 Å compared with those in CYP2B37, with the side chain of F297 assuming an alternate conformation. This marked distortion of the I helix in the CYP2B35 structure (Fig. 6A) from the orientation observed in CYP2B37 or several of the previous CYP2B crystal structures, and the presence of alanine at positions 363 and 367 leads to a significant increase in the active-site volume of CYP2B35. In contrast, in the CYP2B37 active site, the lack of a pronounced kink in the I helix and larger side chains of residues I363 and V367 contributes to a more compact bottom half of the active site

compared with CYP2B35, as shown in Fig. 4D. However, the major residues forming the upper half or roof in the CYP2B37 active site are V104 and I209, compared with I104 and M209 in CYP2B35, which protrude toward the active site. In addition to these substitutions, the F206 side chain flips 90° out of the CYP2B37 active site, opening access to different subchambers adjacent to the main cavity (Fig. 4C). Such rotation of the F206 side chain and that of V104 and I209 in the upper half of the CYP2B37 active site, or the substitution of A363 and A367 in the lower half of the CYP2B35 active site, may orchestrate the differences in binding substrates of various size and shape.

Molecular docking revealed that the narrow bottom half of the CYP2B37 structure appears to strictly constrain longer-chain 7-alkoxycoumarins, even when side chains are allowed to reposition. Binding of these longer 7-alkoxycoumarins was limited to the broader upper half away from the catalytic site. Shorter-chain 7-alkoxycoumarins that include 7-EC and 7-EFC assumed productive binding orientations in the available narrow space near the heme iron in CYP2B37. Movement of the I helix and the residue differences at positions 363 and 367 create a wider space near the heme in the CYP2B35 active site that can accommodate binding of longer-chain 7-alkoxycoumarins in orientations more favorable for proposed metabolism than in the case of smaller substrates. This observation is consistent with previously observed substrate preferences in the CYP2B1 V363A mutant, where an increase in the volume of the active site allows larger substrates to bind in an orientation leading to greater *O*-dealkylation (Kobayashi et al., 1998). In addition, no *O*-dealkylation activity by CYP2B35
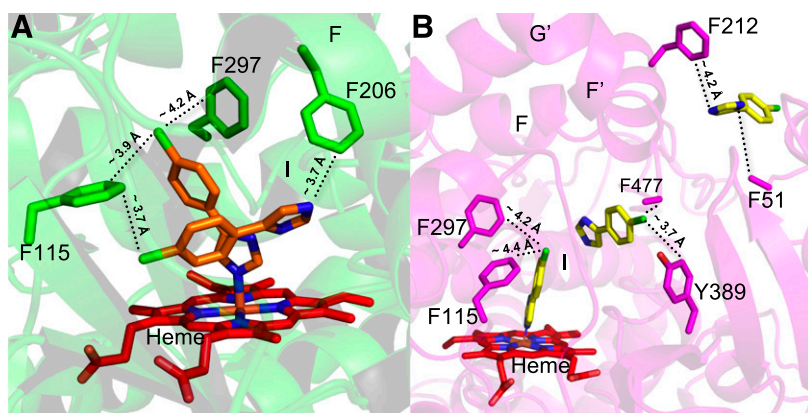

Fig. 7. Demonstration of –Cl- and –NH-π interactions in CYP2B35–4-CPI (green) (A) and CYP2B37–4-CPI (magenta) (B) structures. 4-CPI molecules in the CYP2B35 and CYP2B37 structures are shown as orange and yellow sticks, respectively. Residue side chains of F115, F206, F212, F297, and Y389 that form stable –Cl- or –NH-π interactions are shown as stick representation. The side chains of F51 and F477 that may be involved in such $-\pi$ interactions in the CYP2B37 structure demonstrated disordered electron density, and thus were not modeled. Heme is shown as red sticks.

was observed with the shorter-chain coumarins 7-MFC, 7-EFC, and 7-PrFC, which is consistent with less-favorable docking orientations in the active site. Moreover, CYP2B35 demonstrated increased catalytic efficiency (k_{cat}/K_M) for 7-HpC metabolism by more than 4-fold compared with CYP2B37 (Supplemental Table 1), which could be linked to the differences in the active-site architecture.

More recently, a peripheral pocket adjacent to the active-site I helix and surrounded by residues at positions 180, 188, 194, 195, 198, 199, 202, 241, 244, 245, and 296 was identified that demonstrated binding of the detergent CYMAL-5 in several CYP2B4 and CYP2B6 structures (Jang et al., 2015). Mutations made within this pocket showed significant functional changes that can be related to indirect effects on active-site topology. In the CYP2B35 and CYP2B37 structures, no CYMAL-5 was bound at this peripheral site. To understand the presence or absence of CYMAL-5 binding, the structures of CYP2B35 and CYP2B37 were superimposed onto the representative CYP2B6 and CYP2B4 structures with CYMAL-5 in the pocket. The residues that undergo rearrangement in the presence of CYMAL-5 in the peripheral pocket include 194 located at the entrance of the pocket, and 198, 202, and 296 inside the pocket (Fig. 6B). Rotation of the side chains of residues 194, 198, and 296 to either allow or prevent CYMAL-5 binding might be crucial in determining the access to the pocket in CYP2B4, CYP2B6, CYP2B35, and CYP2B37.

In our recent study (Shah et al., 2015), we proposed that the presence of a –Cl or –NH functional group in a ligand is an important determinant of CYP2B4 or CYP2B6 ligand binding, also shown previously with several crystal structures of protein-ligand complexes (Dougherty, 1996; Dalkas et al., 2014). Several studies in the literature have described the effect of ligands with –Cl and/or –NH functional groups on the formation of stable –π bonds with aromatic side chains via an edge-on or face-on geometry at a distance of 3.7–4.1 Å (Scrutton and Raine, 1996; Imai et al., 2008). A –Cl functional group bound to an aromatic ring, such as the chlorophenyl moiety, has a greater propensity for a stable –Cl-π interaction than a –Cl bound to nonaromatic ligand moieties (Matter et al., 2009). In the CYP2B35 structure, the aromatic ring of the F115 and F297 side chains establishes a –Cl-π bond via edge-on geometry with the 4-CPI molecule that coordinates to heme (Fig. 7A). In addition, the second 4-CPI molecule that occupies the void region near A363 and A367 within the active site of CYP2B35 also participates in –Cl-π or –NH-π interactions with phenylalanine residues F115 or F206, respectively, in the range of 3.7–4.1. In this context, it is noteworthy that concurrent crystallization and structure determination of CYP2B35 with a 1:1 protein:ligand ratio still revealed two molecules of 4-CPI bound within the active site and in similar orientations as those seen in the present structure solved with a 1:10 protein:ligand ratio.

The –π bonding interactions are not limited to CYP2B35, as the –Cl of the 4-CPI coordinated to the heme iron in the CYP2B37 active site interacts with the aromatic side chains of F115 and F297, as shown in Fig. 7B. A second molecule of 4-CPI at the periphery of the active site and in the access channel exhibits a stable –Cl-π interaction with F477 and Y389. Despite the disordered electron density of the F477 side chain at the given resolution in the CYP2B37 structure, the fact that the residue at position 477 is aromatic, as opposed to nonaromatic residues found in CYP2B4 (V477), CYP2B6

(V477), and CYP2B35 (I477), may help to explain the presence of an additional molecule of 4-CPI at this location due to stable –π interactions. Interestingly, a third molecule of 4-CPI located within the previously described *2f* substrate access channel and near the protein surface displays similar –NH-π interactions in a face-on fashion with the F212 side chain, and likely with the F51 side chain, which demonstrated disordered electron density in the crystal structure. Of note, crystallization efforts involving CYP2B37 and 4-CPI at a 1:1 protein:ligand ratio were unsuccessful, suggesting the importance of multiple bound ligands to obtain a stable protein complex. The current results warrant investigation into the role of residues 51 and 477 of CYP2B35 and CYP2B37 in –Cl-π and –NH-π interactions during binding of ligands to the CYP2B subfamily of enzymes, which may further our understanding of such interactions in other P450 enzymes as well.

In conclusion, the CYP2B35 structure demonstrates a distinct active site that preferentially accommodates and metabolizes long-chain coumarin derivatives. In contrast, the active site of CYP2B37 facilitates binding of shorter-chain coumarins. The X-ray crystal structures of these enzymes provide a useful framework to understand the interactions of substrates in the active sites of P450 enzymes with significantly different architectures. Moreover, our results demonstrate the utility of X-ray crystal structures combined with molecular docking in the understanding of metabolism of several series of 7-alkoxy-4–substituted coumarin derivatives of various sizes and shapes. The structures not only helped us to understand the metabolism of coumarin derivatives, but also strengthened our hypothesis proposing a crucial role for –Cl- and –NH-π interactions in CYP2B ligand binding. Site-directed mutagenesis of the key active site residues in the CYP2B35 and CYP2B37 followed by functional and computational analysis may provide further insight into such distinct substrate preferences of these two enzymes.

Authorship Contributions

Participated in research design: Shah, Wilderman, Halpert.
Conducted experiments: Shah, Huo, Liu, Szklarz.
Contributed new reagents or analytic tools: Zhang, Dearing.
Performed data analysis: Shah, Huo, Liu, Wilderman, Szklarz.
Wrote or contributed to the writing of the manuscript: Shah, Huo, Liu, Wilderman, Szklarz, Stout, Halpert.

References

Bailey S; Collaborative Computational Project, Number 4 (1994) The CCP4 suite: programs for protein crystallography. *Acta Crystallogr D Biol Crystallogr* **50**: 760–763.
Battye TG, Kontogiannis L, Johnson O, Powell HR, and Leslie AG (2011) iMOSFLM: a new graphical interface for diffraction-image processing with MOSFLM. *Acta Crystallogr D Biol Crystallogr* **67**:271–281.
Cuff AL and Martin AC (2004) Analysis of void volumes in proteins and application to stability of the p53 tumour suppressor protein. *J Mol Biol* **344**:1199–1209.
Dalkas GA, Teheux F, Kwasigroch JM, and Rooman M (2014) Cation-π, amino-π, π-π, and H-bond interactions stabilize antigen-antibody interfaces. *Proteins* **82**: 1734–1746.
Davis IW, Murray LW, Richardson JS, and Richardson DC (2004) MOLPROBITY: structure validation and all-atom contact analysis for nucleic acids and their complexes. *Nucleic Acids Res* **32**:W615–W619.
Domanski TL and Halpert JR (2001) Analysis of mammalian cytochrome P450 structure and function by site-directed mutagenesis. *Curr Drug Metab* **2**:117–137.
Dougherty DA (1996) Cation-pi interactions in chemistry and biology: a new view of benzene, Phe, Tyr, and Trp. *Science* **271**:163–168.

Emsley P and Cowtan K (2004) Coot: model-building tools for molecular graphics. *Acta Crystallogr D Biol Crystallogr* **60**:2126–2132.

Ericksen SS and Szklarz GD (2005) Regiospecificity of human cytochrome P450 1A1-mediated oxidations: the role of steric effects. *J Biomol Struct Dyn* **23**:243–256.

Gay SC, Roberts AG, and Halpert JR (2010b) Structural features of cytochromes P450 and ligands that affect drug metabolism as revealed by X-ray crystallography and NMR. *Future Med Chem* **2**:1451–1468.

Gay SC, Shah MB, Talakad JC, Maekawa K, Roberts AG, Wilderman PR, Sun L, Yang JY, Huelga SC, and Hong WX et al. (2010a) Crystal structure of a cytochrome P450 2B6 genetic variant in complex with the inhibitor 4-(4-chlorophenyl)imidazole at 2.0-A resolution. *Mol Pharmacol* **77**:529–538.

Gonzalez FJ (1988) The molecular biology of cytochrome P450s. *Pharmacol Rev* **40**:243–288.

Haley SL, Lamb JG, Franklin MR, Constance JE, and Denise Dearing M (2007) Xenobiotic metabolism of plant secondary compounds in juniper (Juniperus monosperma) by specialist and generalist woodrat herbivores, genus Neotoma. *Comp Biochem Physiol C Toxicol Pharmacol* **146**:552–560.

Halpert JR (2011) Structure and function of cytochromes P450 2B: from mechanism-based inactivators to X-ray crystal structures and back. *Drug Metab Dispos* **39**:1113–1121.

Harlow GR, He YA, and Halpert JR (1997) Functional interaction between amino-acid residues 242 and 290 in cytochromes P-450 2B1 and 2B11. *Biochim Biophys Acta* **1338**:259–266.

He YA, He YQ, Szklarz GD, and Halpert JR (1997) Identification of three key residues in substrate recognition site 5 of human cytochrome P450 3A4 by cassette and site-directed mutagenesis. *Biochemistry* **36**:8831–8839.

Hernandez CE, Kumar S, Liu H, and Halpert JR (2006) Investigation of the role of cytochrome P450 2B4 active site residues in substrate metabolism based on crystal structures of the ligand-bound enzyme. *Arch Biochem Biophys* **455**:61–67.

Holmans PL, Shet MS, Martin-Wixtrom CA, Fisher CW, and Estabrook RW (1994) The high-level expression in Escherichia coli of the membrane-bound form of human and rat cytochrome b5 and studies on their mechanism of function. *Arch Biochem Biophys* **312**:554–565.

Huang Q and Szklarz GD (2010) Significant increase in phenacetin oxidation on L382V substitution in human cytochrome P450 1A2. *Drug Metab Dispos* **38**:1039–1045.

Imai YN, Inoue Y, Nakanishi I, and Kitaura K (2008) Cl-pi interactions in protein-ligand complexes. *Protein Sci* **17**:1129–1137.

Jang HH, Davydov DR, Lee GY, Yun CH, and Halpert JR (2014) The role of cytochrome P450 2B6 and 2B4 substrate access channel residues predicted based on crystal structures of the amlodipine complexes. *Arch Biochem Biophys* **545**:100–107.

Jang HH, Liu J, Lee GY, Halpert JR, and Wilderman PR (2015). Functional importance of a peripheral pocket in mammalian cytochrome P450 2B enzymes. *Arch Biochem Biophys* **584**:61–69.

Johnson EF and Stout CD (2013) Structural diversity of eukaryotic membrane cytochrome p450s. *J Biol Chem* **288**:17082–17090.

Kent UM, Hanna IH, Szklarz GD, Vaz AD, Halpert JR, Bend JR, and Hollenberg PF (1997) Significance of glycine 478 in the metabolism of N-benzyl-1-aminobenzotriazole to reactive intermediates by cytochrome P450 2B1. *Biochemistry* **36**:11707–11716.

Kleywegt GJ and Jones TA (1994) Detection, delineation, measurement and display of cavities in macromolecular structures. *Acta Crystallogr D Biol Crystallogr* **50**:178–185.

Kobayashi Y, Fang X, Szklarz GD, and Halpert JR (1998) Probing the active site of cytochrome P450 2B1: metabolism of 7-alkoxycoumarins by the wild type and five site-directed mutants. *Biochemistry* **37**:6679–6688.

Lee SC, Bennett BC, Hong WX, Fu Y, Baker KA, Marcoux J, Robinson CV, Ward AB, Halpert JR, and Stevens RC et al. (2013) Steroid-based facial amphiphiles for stabilization and crystallization of membrane proteins. *Proc Natl Acad Sci USA* **110**:E1203–E1211.

Malenke JR, Magnanou E, Thomas K, and Dearing MD (2012) Cytochrome P450 2B diversity and dietary novelty in the herbivorous, desert woodrat (Neotoma lepida). *PLoS One* **7**:e41510.

Matter H, Nazaré M, Güssregen S, Will DW, Schreuder H, Bauer A, Urmann M, Ritter K, Wagner M, and Wehner V (2009) Evidence for C-Cl/C-Br...pi interactions as an important contribution to protein-ligand binding affinity. *Angew Chem Int Ed Engl* **48**:2911–2916.

McCoy AJ, Grosse-Kunstleve RW, Adams PD, Winn MD, Storoni LC, and Read RJ (2007) Phaser crystallographic software. *J Appl Cryst* **40**:658–674.

Muralidhara BK and Halpert JR (2007) Thermodynamics of ligand binding to P450 2B4 and P450eryF studied by isothermal titration calorimetry. *Drug Metab Rev* **39**:539–556.

Murshudov GN, Vagin AA, and Dodson EJ (1997) Refinement of macromolecular structures by the maximum-likelihood method. *Acta Crystallogr D Biol Crystallogr* **53**:240–255.

Omura T and Sato R (1964a) Carbon monoxide-binding pigment of liver microsomes. I. Evidence for its hemoprotein nature. *J Biol Chem* **239**:2370–2378.

Omura T and Sato R (1964b) Carbon monoxide-binding pigment of liver microsomes. 2. Solubilization purification + properties. *J Biol Chem* **239**:2379–2385.

Ortiz de Montellano PR (2015) *Cytochrome P450: Structure, Mechanism, and Biochemistry*, Kluwer Academic, New York (15).

Paulsen MD and Ornstein RL (1991) A 175-psec molecular dynamics simulation of camphor-bound cytochrome P-450cam. *Proteins* **11**:184–204.

Paulsen MD and Ornstein RL (1992) Predicting the product specificity and coupling of cytochrome P450cam. *J Comput Aided Mol Des* **6**:449–460.

Sánchez-Recillas A, Navarrete-Vázquez G, Hidalgo-Figueroa S, Rios MY, Ibarra-Barajas M, and Estrada-Soto S (2014) Semisynthesis, ex vivo evaluation, and SAR studies of coumarin derivatives as potential antiasthmatic drugs. *Eur J Med Chem* **77**:400–408.

Scott EE, Spatzenegger M, and Halpert JR (2001) A truncation of 2B subfamily cytochromes P450 yields increased expression levels, increased solubility, and decreased aggregation while retaining function. *Arch Biochem Biophys* **395**:57–68.

Scott EE, White MA, He YA, Johnson EF, Stout CD, and Halpert JR (2004) Structure of mammalian cytochrome P450 2B4 complexed with 4-(4-chlorophenyl)imidazole at 1.9-A resolution: insight into the range of P450 conformations and the co-ordination of redox partner binding. *J Biol Chem* **279**:27294–27301.

Scrutton NS and Raine AR (1996) Cation-pi bonding and amino-aromatic interactions in the biomolecular recognition of substituted ammonium ligands. *Biochem J* **319**:1–8.

Segel I (1975) *Enzyme kinetics: Behavior and Analysis of Rapid Equilibrium and Steady-State Enzyme Systems*, Wiley-Interscience, New York.

Shah MB, Jang HH, Zhang Q, David Stout C, and Halpert JR (2013a) X-ray crystal structure of the cytochrome P450 2B4 active site mutant F297A in complex with clopidogrel: insights into compensatory rearrangements of the binding pocket. *Arch Biochem Biophys* **530**:64–72.

Shah MB, Kufareva I, Pascual J, Zhang Q, Stout CD, and Halpert JR (2013b) A structural snapshot of CYP2B4 in complex with paroxetine provides insights into ligand binding and clusters of conformational states. *J Pharmacol Exp Ther* **346**:113–120.

Shah MB, Pascual J, Zhang Q, Stout CD, and Halpert JR (2011) Structures of cytochrome P450 2B6 bound to 4-benzylpyridine and 4-(4-nitrobenzyl)pyridine: insight into inhibitor binding and rearrangement of active site side chains. *Mol Pharmacol* **80**:1047–1055.

Shah MB, Wilderman PR, Liu J, Jang HH, Zhang Q, Stout CD, and Halpert JR (2015) Structural and biophysical characterization of human cytochromes P450 2B6 and 2A6 bound to volatile hydrocarbons: analysis and comparison. *Mol Pharmacol* **87**:649–659.

Shah MB, Wilderman PR, Pascual J, Zhang Q, Stout CD, and Halpert JR (2012) Conformational adaptation of human cytochrome P450 2B6 and rabbit cytochrome P450 2B4 revealed upon binding multiple amlodipine molecules. *Biochemistry* **51**:7225–7238.

Stamp N (2003) Out of the quagmire of plant defense hypotheses. *Q Rev Biol* **78**:23–55.

Strobel SM, Szklarz GD, He Y, Foroozesh M, Alworth WL, Roberts ES, Hollenberg PF, and Halpert JR (1999) Identification of selective mechanism-based inactivators of cytochromes P-450 2B4 and 2B5, and determination of the molecular basis for differential susceptibility. *J Pharmacol Exp Ther* **290**:445–451.

Strong M, Sawaya MR, Wang S, Phillips M, Cascio D, and Eisenberg D (2006) Toward the structural genomics of complexes: crystal structure of a PE/PPE protein complex from Mycobacterium tuberculosis. *Proc Natl Acad Sci USA* **103**:8060–8065.

Szklarz GD, He YA, and Halpert JR (1995) Site-directed mutagenesis as a tool for molecular modeling of cytochrome P450 2B1. *Biochemistry* **34**:14312–14322.

Szklarz GD and Paulsen MD (2002) Molecular modeling of cytochrome P450 1A1: enzyme-substrate interactions and substrate binding affinities. *J Biomol Struct Dyn* **20**:155–162.

Tu Y, Deshmukh R, Sivaneri M, and Szklarz GD (2008) Application of molecular modeling for prediction of substrate specificity in cytochrome P450 1A2 mutants. *Drug Metab Dispos* **36**:2371–2380.

Walsh AA, Szklarz GD, and Scott EE (2013) Human cytochrome P450 1A1 structure and utility in understanding drug and xenobiotic metabolism. *J Biol Chem* **288**:12932–12943.

Weng JK, Philippe RN, and Noel JP (2012) The rise of chemodiversity in plants. *Science* **336**:1667–1670.

Wilderman PR, Gay SC, Jang HH, Zhang Q, Stout CD, and Halpert JR (2012) Investigation by site-directed mutagenesis of the role of cytochrome P450 2B4 non-active-site residues in protein-ligand interactions based on crystal structures of the ligand-bound enzyme. *FEBS J* **279**:1607–1620.

Wilderman PR and Halpert JR (2012) Plasticity of CYP2B enzymes: structural and solution biophysical methods. *Curr Drug Metab* **13**:167–176.

Wilderman PR, Jang HH, Malenke JR, Salib M, Angermeier E, Lamime S, Dearing MD, and Halpert JR (2014) Functional characterization of cytochromes P450 2B from the desert woodrat Neotoma lepida. *Toxicol Appl Pharmacol* **274**:393–401.

Wilderman PR, Shah MB, Jang HH, Stout CD, and Halpert JR (2013) Structural and thermodynamic basis of (+)-α-pinene binding to human cytochrome P450 2B6. *J Am Chem Soc* **135**:10433–10440.

Xiaobing C, Hai-Tao X, Xiao-Qiang S, Ting Z, Qi M, and Yan J (2011) Synthesis and fluorescent probes properties of a coumarin-based piperazine containing fluorine. *Chinese Journal of Organic Chemistry* **31**:544–547.

Zhang H, Gay SC, Shah M, Foroozesh M, Liu J, Osawa Y, Zhang Q, Stout CD, Halpert JR, and Hollenberg PF (2013) Potent mechanism-based inactivation of cytochrome P450 2B4 by 9-ethynylphenanthrene: implications for allosteric modulation of cytochrome P450 catalysis. *Biochemistry* **52**:355–364.

Zhao Y and Halpert JR (2007) Structure-function analysis of cytochromes P450 2B. *Biochim Biophys Acta* **1770**:402–412.

Address correspondence to: Dr. Manish B. Shah, Department of Pharmaceutical Sciences, The University of Connecticut, 69 N Eagleville Road, Unit 3092, Storrs, CT 06269-3092. E-mail: manish.shah@uconn.edu